Journal of Materials Chemistry C

PAPER

Check for updates

Tunable electrochemical doping and charge transport in non-OMIEC:OMIEC blends by microstructure design

Efrat Reyn,[a] Sasha Simotko,[ab] Yogesh Yadav, [ID] [a] Noam Moscovich [ID] [a] and Gitti L. Frey [ID] *[ab]

Organic mixed ionic–electronic conductors (OMIECs) are essential for applications such as organic electrochemical transistors (OECTs), yet inherent structural trade-offs limit the balance between ionic and electronic transport. Here, we demonstrate a microstructure-driven approach to induce and tune mixed conduction in a non-OMIEC n-type fullerene by blending it with a p-type OMIEC polymer. Through systematic variation of blend composition and thermal annealing, we control the blend microstructure and phase separation, gradually transforming the n-type from a purely electron-transporting material into a functional n-type OMIEC. Electrochemical and microstructural analyses reveal that the operating n-type OECT mechanism is enabled by the formation of ion transport pathways by the hydrophilic p-type OMIEC polymer, which mediates the electrochemical doping of the fullerene at polymer: fullerene interfaces. These interfaces are also key for charge transport through the fullerene domains, implying that both electrochemical doping and electron mobility of the fullerene are critically governed by the blend microstructure. Optimal OECT n-type performance is observed for a bulk heterojunction microstructure blend with finely intermixed domains where polymer:fullerene interfaces are maximized, while maintaining continuous pathways for both ionic and electronic carriers in both polarities. Our findings demonstrate that microstructure engineering in blends can enable and control mixed conduction in non-OMIEC materials, offering a synthesis-free and versatile strategy for OMIEC development and integration in OECTs and related bioelectronic platforms.

1. Introduction

The field of organic electronics has seen significant progress in recent years, leading to the development of key technologies such as organic solar cells (OSCs), organic light-emitting diodes (OLEDs), organic field-effect transistors (OFETs), and electrochromic devices. The organic semiconductors used in these applications, primarily conjugated polymers and molecules, offer numerous advantages to their inorganic counterparts, including ease of processing, cost-effectiveness, facile chemical tunability, and mechanical flexibility. These qualities make organic semiconductors highly promising also for use as active materials in bioelectronic applications.[1] The fundamental operating principle in bioelectronics relies on the ability to perform in a biological environment and convert ionic bio-induced signals into electronic signals, and *vice versa*. To meet

this requirement, organic mixed ionic electronic conductors (OMIECs) have been developed, often introducing polar groups to known organic semiconductors. This structure leads to mixed-conduction, where the uptake and transport of ions occur through the polar side chains, while the transport of electronic charges occurs through the π-conjugated backbone.[2,3]

Organic electrochemical transistors (OECTs) are the building blocks of bioelectronic devices and a means to study the ionic–electronic conversion in OMIECs. In OECTs, ions are injected from an electrolyte into the OMIEC channel controlled by a gate electrode, and stabilize electrons or holes that are injected from the source and drain contacts. This process allows charge transport through the channel from source to drain.[4] The figure of merit describing mixed-conduction in OECTs is μC^*, where μ is the electronic charge carrier mobility, and C^* is the volumetric capacitance.[5] Along μC^*, transconductance is also used as a device figure of merit, which depicts the signal amplification of the OECT.

OMIEC materials have generally been synthesized by replacing alkyl side chains in conjugated semiconductors with polar oligo (ethylene glycol) side chains. These modifications

[a] *Department of Materials Science and Engineering, Technion – Israel Institute of Technology, Haifa, 32000, Israel. E-mail: gitti@technion.ac.il*
[b] *The Nancy & Stephen Grand Technion Energy Program, Technion – Israel Institute of Technology, Haifa 32000, Israel*

facilitate the transition of hydrophobic organic semiconductors, traditionally used in OFETs, into materials that exhibit bulk doping, resulting in high volumetric capacitance and transconductance when incorporated into OECTs.[6–9] However, there is usually a structural trade-off between ionic transport and electronic transport. Typically, high electron mobility requires significant crystallinity, while polymers that exhibit high ion conductivity are often amorphous. In addition, the microstructure of an OMIEC film in a dry state can change drastically during device operation due to ion uptake and swelling. This creates an additional challenge, as characterizing the film microstructure using *ex situ* techniques, in conditions that don't simulate the device operating conditions, is not sufficient to predict the effect of the microstructure on device performance. For example, Flagg *et al.* investigated the effect of polymer crystallinity on water uptake in a semiconducting polymer with glycol side-chains, showing that while enhanced crystallinity contributes to higher mobility in OFET conditions (dry state), it causes a decrease in OECT mobility (hydrated state), due to changes in the film microstructure upon ion and water uptake.[10] Szumska *et al.* showed that enhancing ionic uptake by increasing the polar side-chain content can lead to excessive film swelling, resulting in electrochemical instability and deterioration in device performance.[11] Hence, the design of single-component OMIECs remains challenging, as it often necessitates complex and time-intensive synthetic routes, with little to no predictive control over the counteracting effects of microstructural features on ionic and electronic charge transport.

Alternatively, a blend-based approach can be utilized to achieve OMIEC performance without synthesizing new materials, and as suggested here, with minimal structural trade-off between ionic transport and electronic transport. Few examples of using blends to design new OMIECs for OECTs have been reported to date. One study has used a blend of two p-type conjugated copolymers, one hydrophilic and one hydrophobic, to enhance ion transport in OECTs and achieve faster-performing OECTs without compromising the transconductance.[12] Another study employed a similar approach and blended n-type conjugated polymers with oligoglycol and alkyl side chains to enhance OECT performance.[13] A previous study in our group showed that blending poly(3-hexylthiophene) (P3HT), a p-type hydrophobic polymer, with poly(ethylene oxide) (PEO), a polymer electrolyte and an excellent ion conductor, resulted in mixed conductivity controlled by the blend morphology and microstructure.[14] The blending approach has also been recently utilized to achieve ambipolar OECTs, either by blending two OMIEC polymers,[15] or, as has been demonstrated in our group, by blending a p-type polymer and n-type small molecule OMIECs.[16,17] An additional study in our group achieved dual-operation with both electrolyte-gated OFET (EGOFET) and OECT functionalities by blending p-type semiconducting polymer and n-type OMIEC small molecule.[18] Using blends offers great versatility in material selection and offers microstructure tunability through processing conditions. In addition, synergistic effects have been demonstrated in polymer:small-molecule blends for other organic electronic applications, such as OFETs and OSC,[19,20] and have also been observed in polymer:small-molecule blend-based OECTs in our group.[21]
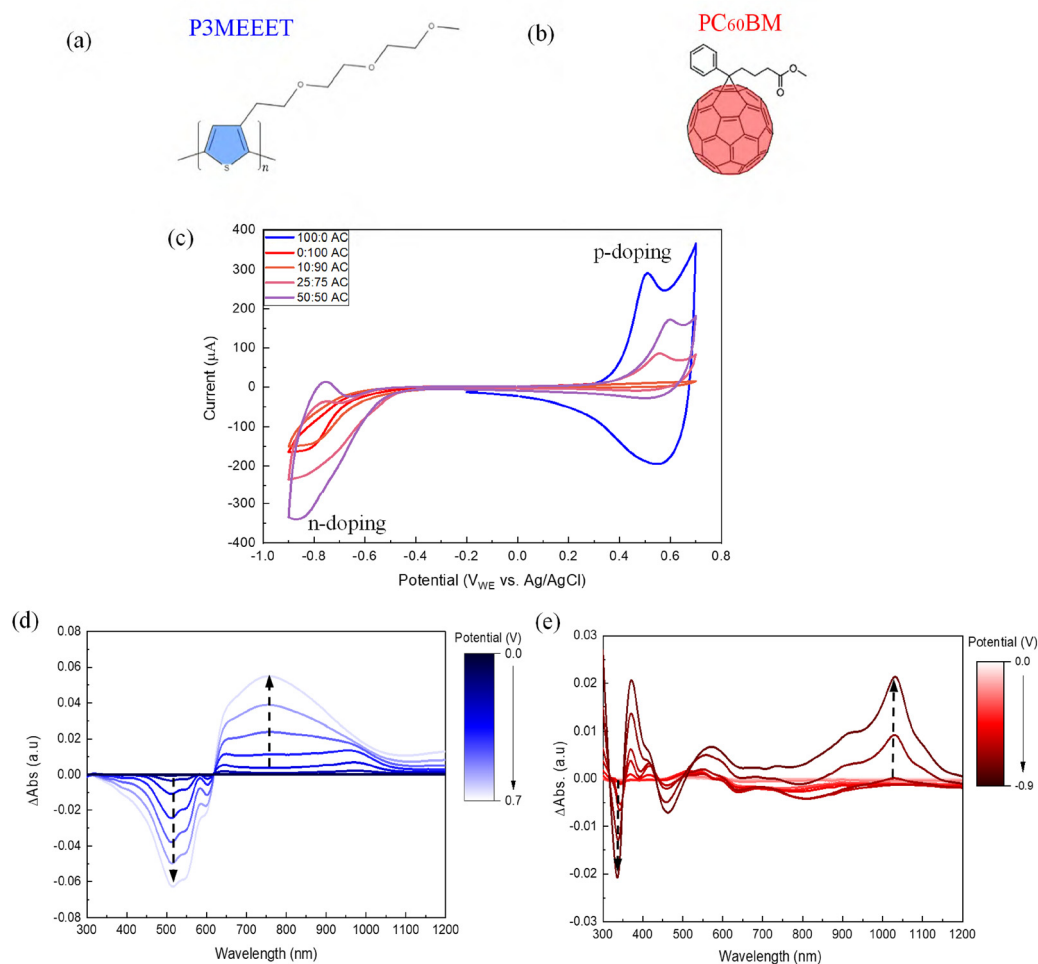
In this work, we suggest harnessing the blend approach to modulate the electrochemical doping and charge transport of a non-OMIEC n-type semiconducting small-molecule by blending it with a p-type OMIEC polymer. We tailor the microstructure of the blend through composition and thermal annealing to achieve a controlled phase separation. We demonstrate that the degree of mixing between the polymer and small-molecule in the blends is the key to tuning the electrochemical doping and charge transport of the small-molecule, effectively enabling its mixed-conductivity in OECTs. By correlating the blend microstructure to the induced mixed-conduction of the small molecule, we aim to expand the range of design tools available for developing OMIEC films. This blending-based strategy allows for the development of OMIECs by microstructure design, avoiding the need for complex chemical modifications of organic semiconductors and thereby simplifying material development and device integration.

2. Results and discussion

To demonstrate that the microstructure of non-OMIEC:OMIEC blends can be harnessed to tune electrochemical doping and charge transport, we selected a blend that, based on our previous experience and expertise, offers microstructure-tunability through composition and thermal treatments. The blend is comprised of a small-molecule fullerene derivative and a polythiophene polymer. Furthermore, to follow charge transport of both positive and negative carriers and both oxidation and reduction doping, the blend components are of opposite polarities, *i.e.*, OMIEC p-type polymer and non-OMIEC n-type fullerene. The selection of a non-OMIEC small-molecule provides two essential points for this study: (i) its electrochemical doping will be associated with the polymer since it cannot transport ions on its own, and (ii) the charge transport properties of a molecular semiconductor strongly depend on molecular packing, orientation and crystallinity, hence offers a sensitive handle to structure–property correlation. By selecting a p-type conjugated OMIEC polymer, rather than relying on a polyelectrolyte for ion transport, we establish an internal reference system that reflects typical OMIEC behavior. By evaluating the performance of the pristine materials and comparing how both the polymer and the fullerene behave in various blend compositions, we gain valuable insights into the structure–performance relationships in OMIECs. The polymer's mixed-conduction properties do not rely on the presence of the fullerene, and we anticipate that following the changes in the p-type performance will complement the trends seen for the fullerene. This parallel observation will help us complete the full picture of the effect of microstructure on the blend performance.

The selected hydrophobic non-OMIEC n-type fullerene-derivative, [6,6]-phenyl C61-butyric acid methyl ester (PC$_{60}$BM)

This journal is © The Royal Society of Chemistry 2026

J. Mater. Chem. C, 2026, **14**, 1164–1176 | 1165

Fig. 1 Chemical structures of (a) P3MEEET and (b) PC$_{60}$BM. (c) Cyclic voltammetry of P3MEEET:PC$_{60}$BM as-cast blends in 0.1 M KCl. The voltammogram corresponds to the 10th scan. (d) and (e) Spectroelectrochemical absorption changes of as-cast 50:50 w:w% blend, measured at +0.7 V to −0.9 with voltage steps of 0.1 V. Blue curves represent the measured absorption changes in positive bias and hence show changes in the polymer doping, while red curves are measured in negative bias and show doping of the fullerene.

(Fig. 1b), is highly popular as the electron acceptor in organic solar cells.[22–24] Although PC$_{60}$BM is a well-known electron transporting material with high electron affinity, it was demonstrated that PC$_{60}$BM doesn't undergo electrochemical doping in aqueous electrolyte within the electrochemical window of water, thus, it cannot operate as a channel material in OECTs.[25] At best, it can be utilized for EGOFETs, where the device operation doesn't involve ion infiltration into the film.[26] The selected p-type component is the OMIEC polythiophene, poly(3-[2-[2-(2-Methoxyethoxy)ethoxy]ethyl]thiophene-2,5-diyl (P3MEEET) (Fig. 1a), which shares the same backbone structure as the benchmark organic semiconductor P3HT, but with glycolated side chains that facilitate ion uptake and transport. P3MEEET showed its mixed-conduction capabilities by demonstrating high values of volumetric capacitance and transconductance when incorporated into OECTs.[8] Similar fullerene:polymer blends have shown a tendency for phase separation and fullerene aggregation,[27,28] controlled by composition and thermal annealing conditions, thus offering several degrees of freedom for microstructure tuning.

To demonstrate that the non-OMIEC fullerene can be electrochemically doped when blended with the polymer, we performed Cyclic Voltammetry (CV) on films of the pristine materials and P3MEEET:PC$_{60}$BM blends in the following compositions: 10:90, 25:75 and 50:50 w:w%. The CV results of the as-cast (AC) pristine materials, Fig. 1c, show that while the polymer undergoes doping and de-doping, evident by the oxidation and reduction peaks in the positive voltages (blue line), the neat fullerene does not (no clear peaks in the negative voltages in the red line). However, introducing the polymer to the fullerene and further increasing its content leads to the appearance of reduction and oxidation peaks in the blends (for example, the magenta line in Fig. 1c). These peaks confirm that electrochemical doping and de-doping of PC$_{60}$BM occur when blended with the polymer, in contrast to the neat fullerene film. The same phenomenon is seen for the thermally annealed (TA) films (Fig. S1), although the redox currents of the fullerene in the blend films are smaller. Doping/de-doping of the polymer, i.e., the redox currents in the positive voltages, follow the polymer content and decrease when the fullerene is added, as

1166 | J. Mater. Chem. C, 2026, 14, 1164–1176

This journal is © The Royal Society of Chemistry 2026

there is a smaller amount of active p-type component to undergo electrochemical doping.

The assignment of the redox peaks in the negative voltages to electrochemical doping of the fullerene in the blend was also confirmed by Spectroelectrochemical (SEC) measurements. The SEC response of the AC and TA pristine films is presented for reference in Fig. S2. The spectra show that pristine polymer films undergo electrochemical doping, while the pristine fullerene films show no significant spectral changes, confirming that $PC_{60}BM$ doesn't undergo electrochemical doping in 0.1 M KCl. In contrast to the pristine fullerene films, the SEC response of the 50:50 w:w% AC blend shows electrochemical doping of both the polymer in positive voltages (Fig. 1d) and the fullerene in negative voltages (Fig. 1e). For the fullerene, a broad peak in the near infrared range is formed, consistent with previously reported absorption spectra of C_{60}^- anion in solution, confirming the formation of a fullerene radical anion.[29] SEC results support the redox peaks obtained in the CV measurements and confirm that upon blending with the OMIEC polymer, the non-OMIEC fullerene can undergo electrochemical doping.

To analyze the doping behavior of the fullerene and the polymer across all blend compositions, the absorption changes at λ = 787 nm (polymer polaron) and λ = 1028 nm (fullerene radical anion) at the highest doping potentials for each component (+0.7 V for the polymer and −0.9 V for the fullerene) in the blend are calculated with respect to the recorded spectrum at V_{WE} = 0 V, where both components are undoped (full SEC results for all blend compositions are shown in Fig. S3 and S4). Therefore, only the contribution of newly formed doped states is taken into consideration. These changes in absorption are proportional to the number of doped states formed under the applied potential, effectively reflecting the doping level of each component in the blend. The absorption changes as a function of polymer content in the blend are presented in Fig. 2, for both AC and TA films.

An opposite trend in the electrochemical doping of the polymer and the fullerene as a function of their content in the blend can be seen in Fig. 2. At first glance, the expected trend is obtained for the polymer, where increasing the polymer content in the blend also increases the p-doping level, for both the AC and TA films (Fig. 2a). A closer look reveals that the p-doping doesn't change linearly with the polymer's content. For example, decreasing the polymer content from 100 wt% to 50 wt% leads to a decrease of more than 2-fold in the formation of the polaron peak. This result suggests that the fullerene's hydrophobic nature interferes with the polymer's electrochemical doping process, by hindering the infiltration of ions into the film and limiting their access to the polymer. On the other hand, a counterintuitive trend is obtained for the fullerene, where a decrease in the fullerene content (i.e., an increase in polymer content) actually leads to a rise in the n-doping level, Fig. 2b. We hypothesize that the polymer's glycolated side chains support not only the transport of anions for self-doping (under positive bias), but also the transport of cations (under negative bias), enabling the volumetric doping of the fullerene. The mutual impact of the polymer and fullerene on each other's doping behavior suggests that the extent of their mixing affects the doping processes of both components, since ionic–electronic coupling requires the ionic and electronic charges to be in close proximity to enable electrostatic charge compensation. Thermal annealing also affects the doping levels, causing a drastic decrease in the fullerene's doping in all blend compositions, while leading to an increase in the polymer's doping. These trends suggest that other factors, beyond the blend composition, tune the electrochemical doping of both blend components.

This led us to investigate the microstructure of the blend, as a function of composition and thermal treatment, and its effect on the doping behavior of both components. We apply the Vapor-Phase infiltration (VPI) process using diethyl zinc and water to reveal the phase separation via High-Resolution Scanning Electron Microscopy (HRSEM) imaging. In VPI, the precursors of a metal oxide, in this case ZnO, selectively infiltrate less dense phases, generally polymer domains, while the infiltration is hindered for the more dense fullerene phase.[30] Accordingly,
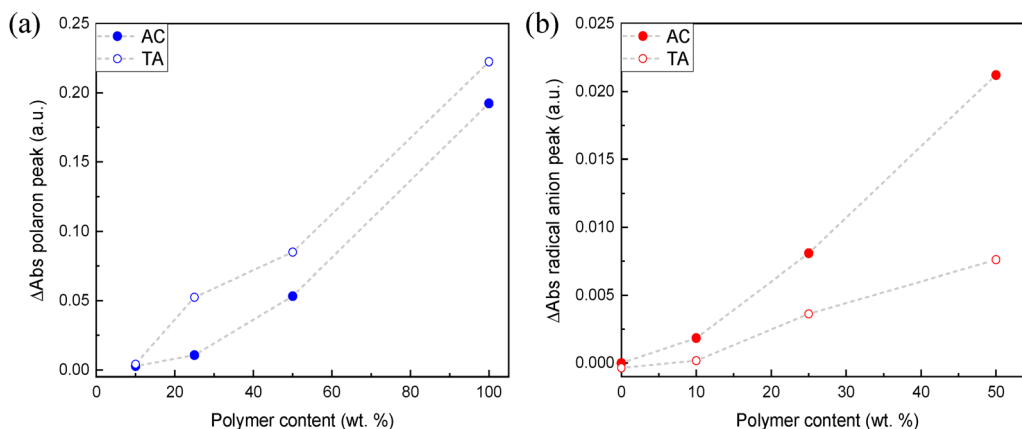

Fig. 2 Absorption changes at: (a) λ = 787 nm, i.e. polymer polaron, and (b) λ = 1028 nm, i.e. fullerene radical anion, at the respective highest doping voltages (+0.7 V for the polymer and −0.9 V for the fullerene) as a function of blend composition for the as-cast and thermally annealed films.

Back Scattered Electron (BSE) HRSEM cross-section images of pristine polymer film show bright contrast representing selective sub-surface ZnO deposition (Fig. S5a). In contrast, the cross-section images of pristine $PC_{60}BM$ films are dark due to hindered precursor infiltration into the film (Fig. S5b). This Z-contrast between the polymer and the fullerene allows us to distinguish the two phases in the blends, where fullerene-rich domains are dark, polymer-rich domains are bright, and grey areas are mixed domains.[28]

The BSE HRSEM cross-section images of $P3MEEET:PC_{60}BM$ blend films are presented in Fig. 3. The blends present varied microstructures as a function of blend composition and thermal treatment. For example, the AC films show that the $10:90$ w:w% $P3MEEET:PC_{60}BM$ blend forms a bilayer-like structure with the polymer preferentially at the surface. The $25:75$ w:w% blend forms a lateral phase separation with fullerene-rich domains (seen as dark islands) surrounded by a mixed phase (seen in grey). The $50:50$ w:w% blend is characterized by high intermixing, possibly forming a bulk heterojunction (BHJ) microstructure, which is known to be the optimized structure for charge separation and transport in OSC. After thermal annealing, an extensive micron-long phase separation can be seen for all blend compositions.

The blend that exhibits the highest mixing of the polymer and the fullerene, *i.e.*, the AC $50:50$ w:w% blend, also shows the highest level of electrochemical doping of the fullerene, as measured by SEC (Fig. 2b). The AC polymer:fullerene $25:75$ w:w% blend, where phase separation is seen, shows more than a 2-fold reduction in the fullerene doping compared to the $50:50$ w:w% blend, even though the fullerene content is 1.5 times higher. A similar observation can be made when comparing the TA and AC films. The annealed blends, which display a lower degree of mixing, evident in the HRSEM images, also show reduced fullerene doping compared to the corresponding AC films with more mixing. Thus, when correlating the observed microstructure with the trends in the SEC measurements, we can conclude that fullerene doping depends not only on the polymer content in the blend, but also on the degree of mixing. In particular, the formation of well-distributed $P3MEEET:PC_{60}BM$ interfaces,

promoted by a finely intermixed microstructure, is critical for effective electrochemical doping of the fullerene.

After establishing the role of the blend microstructure on the electrochemical doping process of the fullerene in the blends, we moved to investigate its effect on the charge transport process. OECTs were fabricated and tested in both p-type and n-type operation regimes. The pristine AC and TA $PC_{60}BM$ films, although good n-type materials for OFETs, showed no n-type OECT performance (Fig. S6), in agreement with previous reports.[25] The pristine AC P3MEEET showed good OECT p-type performance, which improved after thermal annealing (Fig. S7).

In the AC blends, adding P3MEEET to the fullerene induced the previously inaccessible $PC_{60}BM$ OECT n-type performance, already at a concentration of 10 wt% polymer (Fig. S8). Increasing the polymer content to 25 wt% and 50 wt% led to an increase in both n-type and p-type drain currents, with the $50:50$ w:w% blend exhibiting currents in the same order of magnitude for both polarities. The n-type performance observed in the AC films indicates that $PC_{60}BM$ effectively functions as an n-type OMIEC in the blends. We propose the following mechanism for $PC_{60}BM$ in AC blend-based OECTs: (i) cations injected from the electrolyte into and through the polymer-rich domains electrochemically dope the fullerene at the polymer:fullerene interfaces in the blends, and (ii) the microstructure, tuned by blend composition, directs the degree of phase separation and hence the polymer:fullerene interfacial area for doping and the formation of continuous pathways for electronic charge transport through fullerene domains.

In OECTs based on the TA blends, no n-type performance was recorded regardless of composition, while for the p-type, the measured drain currents increased in all blend compositions compared to the equivalent AC films (Fig. S8). The diminished fullerene doping observed in the TA films is unlikely to be the sole reason for the complete suppression of n-type currents. A gradual reduction in doping would typically result in a proportional decrease in drain currents, not an abrupt elimination. Instead, we propose that the strong phase separation, clearly visible in the HRSEM images (Fig. 3b), is the primary contributor to this behavior by effectively blocking
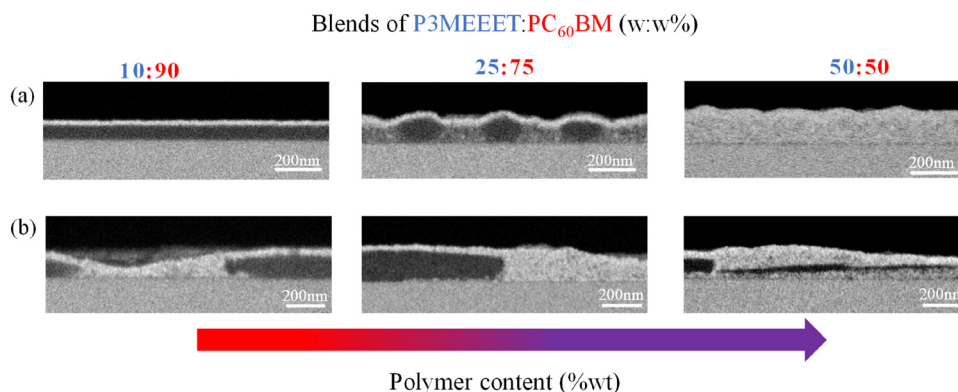

Blends of P3MEEET:PC_{60}BM (w:w%)

Fig. 3 Cross-section BSE HRSEM micrographs of (a) as-cast and (b) thermally annealed P3MEEET:PC_{60}BM films of different blend compositions after VPI staining. The bright contrast is associated to the polymer domains, the dark contrast to the fullerene domains.

1168 | *J. Mater. Chem. C*, 2026, **14**, 1164–1176

This journal is © The Royal Society of Chemistry 2026

charge transport of electrons between the separated fullerene domains.

Both electrochemical doping and charge transport, the two processes that dictate OECT performance, are sensitive to molecular ordering, often enhanced by thermal treatment.[31–33] Increased molecular order enhances charge transport within the film by providing more efficient pathways for electronic charge conduction.[34,35] Moreover, greater crystallinity of the OMIEC material can reduce both passive and active swelling, which enables better ionic–electronic coupling, and supports the continuity of crystalline domains.[36] Therefore, we utilized Grazing Incidence Wide-Angle X-Ray Scattering (GIWAXS) to investigate the effect of thermal treatment on the blends' crystallinity and orientation, and correlate it to the device performance.

Pristine polymer films, AC and TA, display some degree of crystallinity, evident by the diffraction peaks associated with the (h00) lamellar reflections of P3MEEET (Fig. S9), with higher intensities in the out-of-plane direction, indicating a favorable edge-on orientation.[8] After annealing, the increase in peaks' intensity and sharpness indicates higher crystallinity of the polymer film. The enhanced crystallinity of the TA pristine polymer film may account for the increased p-doping (Fig. 2a) and the improved p-type performance in OECTs (Fig. S7). The GIWAXS patterns of the pristine fullerene films, both AC (Fig. S10) and TA (Fig. 4), indicate that $PC_{60}BM$ is generally amorphous with possible small crystallites randomly oriented, evident by the broad isotropic rings at $q \sim 7.5$ nm^{-1} and $q \sim 12.9$ nm^{-1}, in agreement with previous reports.[37] We can conclude that the chosen annealing temperature, 120 °C, together with the short annealing time (20 min), was not enough to induce crystallinity in the pristine $PC_{60}BM$, which is known to crystallize at higher temperatures.[38]

Moving to the blends, the addition of the polymer to the fullerene in the AC films does not change the fullerene reflections, maintaining the same broad isotropic diffraction rings

seen in all blend compositions (Fig. S9). For the polymer, obvious diffraction peaks appear only in the 50:50 w:w% blend in the out-of-plane direction and are correlated to the (h00) lamellar spacing. Upon thermal annealing, the polymer lamellar peaks become more distinct and show higher intensity, even in fullerene-rich blends (Fig. 4), indicating increased polymer crystallinity in the TA blends compared to the AC ones. Similar to the pristine polymer films, the thermal treatment enhances the p-doping and OECT p-type performance in the blends (Fig. S8) and is associated with increased polymer crystallinity. The phase-separated microstructure observed in all blend compositions after annealing (Fig. 3b) may also contribute to the improved p-type performance. The reduced mixing and the formation of distinct polymer and fullerene domains in the TA blends minimize the fullerene's interference with ion uptake, thereby enhancing ion accessibility to the polymer domains.

The impact of thermal annealing on the crystallinity of the fullerene in the blends is even more significant. The low-intensity isotropic rings obtained for the TA pristine fullerene film transform into distinct crystalline peaks in the 50:50 w:w% blend (highlighted in white rectangles in Fig. 4), associated with the formation of $PC_{60}BM$ oriented crystallites. The formation of these peaks indicates that blending the polymer with the fullerene and annealing the films induce both crystallization and orientation of the fullerene. Wang et al. observed a similar effect in P3HT:$PC_{60}BM$ blends, where fullerene crystallization was induced by solvent vapor post-treatment.[39] Verploegen et al. also reported a comparable effect on fullerene crystallinity upon thermally annealing a P3HT:$PC_{60}BM$ blend (25:75 w:w%) at 220 °C, though with a less preferred orientation of the fullerene crystallites.[38] Another study thoroughly investigated the miscibility and aggregation of $PC_{60}BM$ in P3HT:$PC_{60}BM$ blends, suggesting that the crystallization of P3HT leads to segregation of $PC_{60}BM$ from the amorphous regions of the polymer when crossing a miscibility threshold, leading to fullerene aggregation and crystallization.[40]
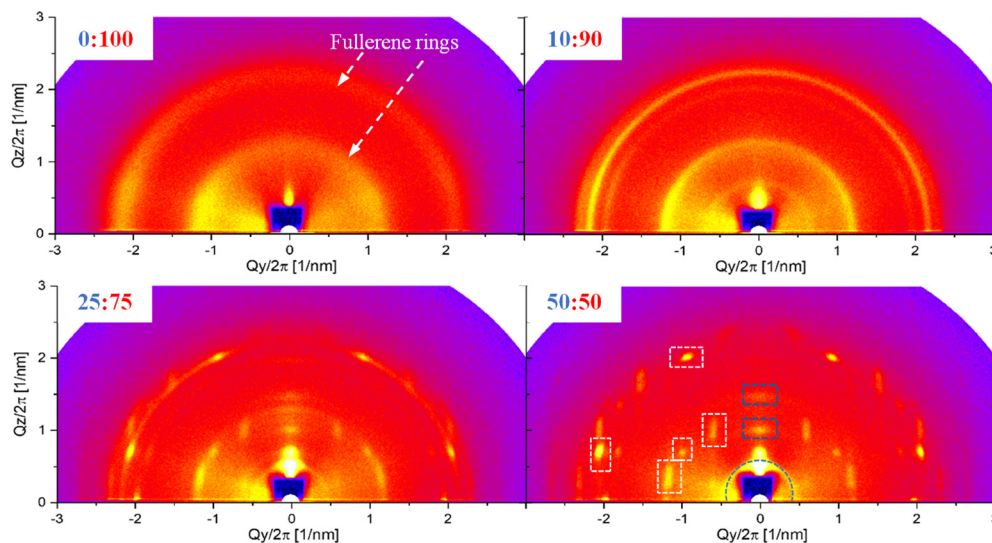

Fig. 4 2D–GIWAXS patterns of thermally annealed P3MEEET:$PC_{60}BM$ blends. Crystalline fullerene peaks are marked in white, and polymer peaks in blue.

This journal is © The Royal Society of Chemistry 2026

J. Mater. Chem. C, 2026, 14, 1164–1176 | 1169

We propose that, in a manner analogous to how P3HT crystallization drives fullerene aggregation in P3HT:PC$_{60}$BM blends, the crystallization of P3MEEET, as evident from the GIWAXS of both the pristine TA polymer film (Fig. S8) and the TA blends (Fig. 4), is the driving force for the formation of the separated, ordered fullerene crystallites observed in the P3MEEET:PC$_{60}$BM TA blends. A complete understanding of the fullerene's induced crystallization in our system requires further investigation, which is beyond the scope of this study.

The substantial effect of thermal treatment on the molecular order of PC$_{60}$BM in the blends is expected to improve the electron mobility and increase the n-type performance in OECTs compared to the AC blends. However, all the TA blends showed no n-type performance. These results indicate that n-type performance in the TA blends is determined primarily by phase continuity, rather than by the degree of crystallinity of the fullerene domains. Therefore, the enhanced molecular order of PC$_{60}$BM does not improve the n-type electrical performance of the TA blends, as it is overshadowed by the formation of large, isolated fullerene domains (Fig. 3b) that fail to establish a continuous pathway for charge transport. The pronounced sensitivity of PC$_{60}$BM to phase continuity reflects its high percolation threshold for electronic charge transport, consistent with previous reports on blend-based ambipolar OFETs.[41,42] Notably, P3MEEET retains its electrical performance in TA blends even at low polymer content (10 : 90 w : w%), despite the pronounced phase separation. This observation is in agreement with prior studies demonstrating that semiconducting polymers can sustain charge mobility in blend-based OFETs[43,44] and OECTs[16] at very low content, indicative of a low percolation threshold.

The absence of electron-transporting pathways, and hence the lack of n-type OECT performance, in all TA blends leads us to analyze the induced n-type performance of the fullerene in the AC blends. More particularly, we want to understand how the blend composition and microstructure affect volumetric capacitance (C^*) and electron mobility (μ), the two parameters defining the device performance and reflecting the material's ability to act as an OMIEC in OECTs. To extract values for the volumetric capacitance of each component in the blend, we performed Electrochemical Impedance Spectroscopy measurements (EIS) for the pristine materials and the blend films. We calculated C^* from the extracted effective capacitance (see Experimental section) by dividing it by the estimated volume of the film. The C^* values are calculated at the highest doping potentials of each component, +0.7 V for the polymer and −0.9 V for the fullerene (Table S1). To calculate the mobility, μ, we extracted the μC^* product and divided it by the calculated C^* values. Since volumetric capacitance reflects the bulk properties of the OMIEC film, and each component, polymer or fullerene, undergoes doping and contributes to the overall capacitance at different doping potentials, we normalized the extracted C^* values by wt% to receive the effective p-type and n-type capacitance.[21] The normalized volumetric capacitance represents the C^* of each component in the blend, as if the whole film were composed of a single OMIEC material.

We calculated the volumetric capacitance of the pristine PC$_{60}$BM film, considering its whole volume, despite the fact that it does not undergo volumetric doping when not blended with the polymer (see SI for a more detailed explanation). This was done for comparative reasons, and similarly to our calculation for the polymer (which does undergo volumetric doping), to demonstrate the transition of PC$_{60}$BM from a non-OMIEC to an OMIEC material when blended with the polymer.

Fig. 5 shows the polymer and fullerene normalized volumetric capacitance and the p-type and n-type mobilities as a function of blend composition. The normalized volumetric capacitance varies with blend composition in a manner similar to the trends obtained in Fig. 2 for the SEC measurements. Namely, the values increase for both the polymer and the fullerene with polymer content (Fig. 5a). This is anticipated because a variation in the number of doped states (the emergence of a positive polaron peak or radical anion peak) at a specific potential reflects the charges induced per unit voltage. When normalized per unit volume of the OMIEC film, this value defines volumetric capacitance. Therefore, the notable decrease in p-type normalized capacitance with increasing fullerene content in the blend corresponds with the SEC results. This further highlights the considerable interfering effect that PC$_{60}$BM has on the polymer's electrochemical
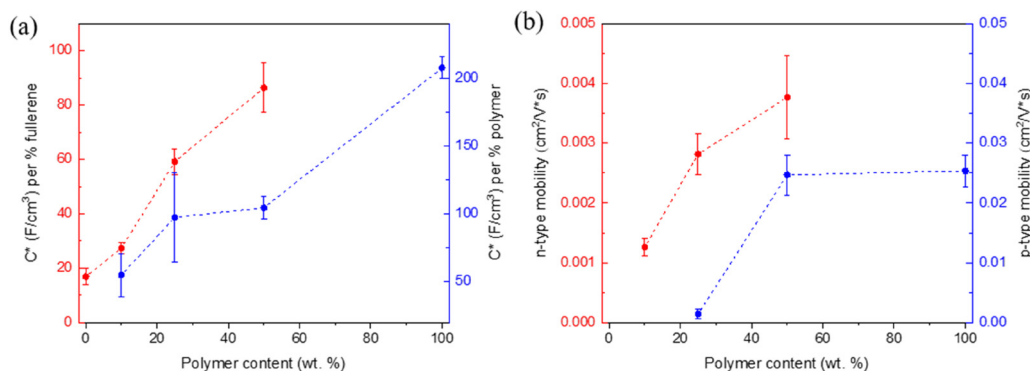

Fig. 5 (a) Normalized volumetric capacitance and (b) mobility of the fullerene (red) and the polymer (blue) as a function of polymer content in the as-cast films.

doping and capacitive ability. Similarly, the increase in the n-type normalized capacitance is directly linked to the increased fullerene doping supported by the polymer.

The 50:50 w:w% AC blend, exhibiting the highest fullerene doping levels, also demonstrates the highest n-type capacitance per wt% of fullerene, with C^* of 86 ± 9 F cm^{-3} per %. This value is in the same order of magnitude as the value measured for PrC$_{60}$MA (C60,N,N,N-trimethyl-1-(2,3,4-tris(2-(2-methoxyethoxy)-ethoxy)phenyl)methanaminium monoadduct), an n-type OMIEC fullerene derivative with glycolated side-chains, which was successfully incorporated into OECTs.[21] This suggests that the high level of mixing and the formation of numerous P3MEEET:PC$_{60}$BM interfaces in the 50:50 w:w% AC blend, allow cations and electrons, though spatially separated between the two phases, to couple as effectively as if the glycolated side-chains were directly attached to the PC$_{60}$BM.

While the polymer side chains can support ionic transport for both p-type (anions) and n-type (cations) activity, electronic charge transport occurs through the conjugated system, where the transport of holes is supported by the polymer, and the transport of electrons is supported by the fullerene. Hence, the mobility of the charge carriers depends on the content of the conjugated p-type or n-type material in the blend. For the polymer, the p-type mobility in the AC blends reduces as expected with decreased polymer content, though not gradually (Fig. 5b). At 50 wt% polymer, p-type mobility remains unchanged compared to the pristine polymer film, but a significant drop occurs at 25 wt%, with no p-type performance in AC blends below this concentration. This decrease in hole mobility is attributed to the higher fullerene content, which leads to less interconnected polymer chains and impedes effective charge transport.

The changes in the n-type mobility resulting from variations in blend composition are less predictable. Interestingly, n-type mobility increases with the polymer content, despite a concurrent decrease in the fullerene concentration. This, together with a greater degree of mixing with the polymer as its content rises, is expected to reduce electron mobility through the fullerene domains by hindering continuous transport pathways. To resolve this contradiction, we need to account for the dependence of mobility on charge carrier concentration, which is non-monotonic in disordered organic semiconductors. In low carrier concentration, the transport is governed by trap filling, and the mobility is almost constant. At higher charge carrier concentration, only part of the carriers are trapped while the remaining ones are free to transport by hopping between available states, leading to an increase in mobility.[45] This behavior was also demonstrated for OMIECs incorporated into electrochemically-gated transistors.[46]

In our system, the increase in polymer content in the blend enhances the doping of the fullerene, thereby raising the charge carrier concentration. Thus, the increase in the n-type mobility with the increase in the polymer content is attributed to the higher charge carrier concentration available for transport. This interpretation is supported by the absence of any detectable changes in the fullerene's crystallinity within the AC blends, ruling out the formation of a more favorable microstructure for electron transport as a contributing factor.
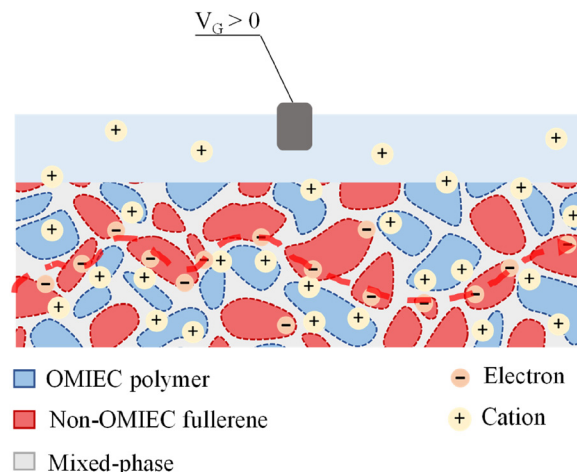

Fig. 6 A scheme of the OECT operation mechanism for the fullerene in P3MEEET:PC$_{60}$BM blends. The red arrow indicates the pathway for electronic charge transport through the fullerene domains.

The maximum value of electron mobility, $\sim 3.8 \times 10^{-3}$ cm^2 V^{-1} s^{-1}, was achieved for the 50:50 w:w% AC blend. This value is higher than the n-type mobilities of reported non-fullerene small-molecule semiconductors-based OMIECs,[47] but one order of magnitude lower than C$_{60}$TEG[25] (2-(2,3,4-tris(methoxtriglycol)phenyl)[60]fulleropyrrolidine) and 2 orders of magnitude lower than PrC$_{60}$MA.[21] Their relatively high mobility stems from their highly ordered and crystalline molecular packing (after thermal annealing). By comparing the n-type mobilities measured for PC$_{60}$BM in the AC blends with the two aforementioned fullerene derivatives, we can identify that the limiting factor for n-type charge transport in the AC P3MEEET:PC$_{60}$BM blends is the amorphous, non-oriented structure of PC$_{60}$BM.

Our findings reveal that both the electrochemical doping and charge transport of PC$_{60}$BM are critically controlled by the formation of P3MEEET:PC$_{60}$BM interfaces. The operating mechanism of PC$_{60}$BM in OECTs is illustrated in the scheme in Fig. 6. At positive gate voltages, cations are injected into the film and infiltrate through the polymer domains, coupling with electrons at polymer:fullerene interfaces, thus enabling electron transport through continuous fullerene domains. These optimal conditions are met in the 50:50 w:w% AC blend, where a BHJ microstructure not only maximizes the P3MEEET:PC$_{60}$BM interfacial area, but also offers interconnected networks of both components. This microstructure supports continuous transport pathways for holes through the polymer domains and electrons through the fullerene domains, resulting in the highest n-type volumetric capacitance n-type mobility.

3. Conclusions

In this work, we showed that blending a non-OMIEC hydrophobic fullerene, PC$_{60}$BM, with an OMIEC polymer, P3MEEET, enables the transformation of PC$_{60}$BM from an electron-conducting material only to an n-type OMIEC, capable of

This journal is © The Royal Society of Chemistry 2026

J. Mater. Chem. C, 2026, 14, 1164–1176 | 1171

functioning as an active channel material in OECTs. The induced electrochemical doping of the fullerene is governed by the formation of polymer:fullerene interfaces, where cations transported through the polymer phase stabilize electrons in the fullerene phase at the interface of the two phases. Hence, we demonstrate that the electrochemical doping of the fullerene can be tuned through blend composition and thermal annealing. Additionally, the electron mobility of the fullerene in the blends depends on the available electronic charge carriers, which increase with the level of fullerene doping. Therefore, electron mobility is also governed by the degree of mixing of the polymer and the fullerene, and is limited by the continuity and crystallinity of the fullerene phase. We find that the optimal blend for the highest doping efficiency and charge transport of $PC_{60}BM$ is a 50:50 w:w% AC blend, where a BHJ microstructure maximizes the polymer:fullerene interfaces, allowing efficient fullerene doping, while maintaining interconnected pathways for charge transport in both polarities. We've also illustrated that thermal annealing induces crystallization and orientation of the fullerene in the blends, providing an additional strategy to enhance charge transport in blend-based OECTs. Although the volumetric capacitance and electron mobility of $PC_{60}BM$ in our system do not reach state-of-the-art values, our findings demonstrate that both electrochemical doping and charge transport can be effectively modulated through careful control of blend composition and microstructure. This approach broadens the range of tools available for designing new OMIEC materials and enables the tuning of mixed-conduction properties, crucial for device optimization. Further research should focus on understanding how blending non-OMIEC and OMIEC materials affects the swelling behavior of the film, as well as the dynamics of ionic and electronic charge transport. Such insights may reveal additional synergistic effects and functionalities, including enhanced stability and selective ion sensitivity.

4. Experimental: materials and methods

4.1. Materials

Poly(3-[2-(2-methoxyethoxy)ethoxy]ethylthiophene-2,5-diyl) (P3MEEET, Mn = 8 kD, M_w = 12 kD, D = 1.6, regioregularity = 87%, Rieke Metals), [6,6]-phenyl C61-butyric acid methyl ester ($PC_{60}BM$, 99.5% purity, Nano-C), potassium chloride, KCl (Sigma-Aldrich Israel Ltd), diethylzinc, DEZ (packaged for use in deposition systems, Sigma-Aldrich Israel Ltd), chloroform (anhydrous, ≥99%, Sigma-Aldrich Israel Ltd) were purchased and used as received.

4.2. Sample preparation

All substrates were cleaned before film deposition in an ultrasonic bath in acetone, methanol, and isopropanol (15 minutes each) and blow-dried in N_2 (99.995%). P3MEEET and $PC_{60}BM$ were dissolved in chloroform at concentrations of 10 mg ml^{-1} at room temperature, and stirred for at least 3 hours before further processing. For blend preparation, pristine material solutions were mixed in the appropriate amounts to achieve 10:90, 25:75, and 50:50 (w:w%) blend ratios, at a concentration of 10 mg ml^{-1}. All solutions were spin-coated at room temperature onto substrates at 1000 rpm for 60 s, followed by 2000 rpm for 10 s, to obtain 50–60 nm film thicknesses for the pristine materials and 65–75 nm for the blends. For VPI measurements, we prepared thicker films, ∼110 nm, using 700 rpm for 60 s with the above solutions.

The thermally annealed films were subsequently annealed on a hot plate at 120 °C for 20 minutes.

Film preparation was executed entirely under an inert atmosphere inside a glovebox. Film thicknesses were measured using a stylus profilometer (Bruker DektakXT) with a 12.5 μm radius of the needle tip.

4.3. Cyclic Voltammetry (CV) and Spectroelectrochemistry (SEC)

For SEC, fluorine-doped tin oxide (FTO) coated glass (surface resistivity ∼7 Ω sq^{-1}, Sigma-Aldrich Israel Ltd) was used as a conductive transparent working electrode (WE) and coated with materials as described above. The FTO-coated substrates were dipped in a 0.1 M KCl solution in a glass cuvette (3/G/10, Starna Scientific Ltd) with a platinum (Pt) wire as counter electrode (CE) and an Ag/AgCl sintered pellet (NS7671, NEUROSPEC) reference electrode (RE). To avoid faradaic side reactions on the FTO surface, the edges of the substrate were masked with Kapton® tape. This setup was placed in a UV-VIS-NIR spectrophotometer (Cary 5000 Scan, Agilent Technologies, Inc.) and connected to an external potentiostat (Palmsens4, PalmSens BV). A series of spectra were acquired at step voltages ranging from +0.7 V to −0.9 V, where each voltage step was held constant for 210 s. Absorbance changes were calculated with respect to V_{WE} = 0 V. For CV measurements, the same set-up was used, and 10 cycles were performed in the range of +0.3 V → −0.9 V for $PC_{60}BM$, −0.2 V → +0.7 V for P3MEEET, and +0.7 V → −0.9 V for the blends, at a rate of 0.1 V s^{-1}.

4.4. Device fabrication and measurements

A 4-inch glass wafer was first cleaned and treated with hexamethyldisilazane (HMDS), followed by spin-coating with AZ5214E photoresist. The photoresist was exposed to 375 nm UV light using a mask-less exposure system (MLA 150, Heidelberg Instruments) to define source and drain patterns. After the development of the photoresist, a metal stack of 5 nm Cr and 50 nm Au was deposited via e-beam evaporation. The lift-off process removed the photoresist, leaving the patterned metal contacts. Two layers of polyimide were then successively deposited: the first serving as a protective layer for the metal contacts and the second as a sacrificial layer. After curing the polyimide, a photoresist (AZ4562) was applied, exposed, and developed to define the device channel patterns. The sacrificial polyimide layer was subsequently etched by reactive ion etching to partially expose the source and drain contacts (to a thickness of ∼500 nm). Finally, after spin-coating the organic material, the sacrificial layer was peeled off, completing the OECT fabrication process. This process was employed to fabricate devices

1172 | J. Mater. Chem. C, 2026, **14**, 1164–1176

This journal is © The Royal Society of Chemistry 2026

with interdigitated channels featuring a channel width of $W = 6000$ μm and a channel length of $L = 30$ μm, with each substrate containing 4 pixels.

The characterization of the devices was performed using a dual-channel source measure unit (SMU) (B2902A, Keysight Technologies, Inc.), controlled via dedicated software (Easy-Expert Group+). The SMU was connected to the source and drain gold contacts, as well as to an Ag/AgCl pellet. Transfer curves were measured in 0.1 M KCl by a double-sweep (forward and backward) of the gate voltage (V_G), with a constant source-drain voltage (V_D). For a p-type scan, V_G was swept with a step size of 1 mV at a scan rate of ~ 0.01 V s^{-1} between 0 V to -0.7 V at a $V_D = -0.3$ V. For an n-type scan, V_G was swept with a step size of 1 mV at a scan rate of ~ 0.01 V s^{-1} between 0 V to $+0.9$ V at a $V_D = +0.3$ V.

Results were analyzed based on the average of 6–8 devices per composition. To extract μC^* values, the following equation was used:

$$g_m = \frac{\partial I_D}{\partial V_G} = \frac{Wd}{L}|V_G - V_{th}| * \mu C^* \tag{1}$$

The threshold voltage (V_{th}) was calculated by determining the x-intercept of a linear fit of $\sqrt{I_D}$ vs. V_G based on the forward scan of the transfer curve.

4.5. Electrochemical Impedance Spectroscopy (EIS)

Cr/Au square pads (0.0036 cm^2) were photolithographically patterned on a microscope glass slide using a method explained elsewhere[48] and spin-coated with the semiconductor solution in chloroform, followed by peeling of a top sacrificial layer of Parylene C. The impedance spectra were recorded with a Potentiostat (PalmSens4, PalmSens BV) in a 3-electrode setup using a 0.1 M KCl solution, Ag/AgCl pellet as RE, and Pt wire as CE, at a frequency range between 1 MHz and 0.1 Hz. The measurements were performed at DC voltage ranging from $+0.7$ V to -0.9 V with a step of 0.1 V, and AC amplitude of 10 mV.

The capacitance was calculated from the effective capacitance (at 1 Hz) given by the following equation:

$$C_{eff} = -\frac{1}{2\pi f Z''} \tag{2}$$

where f is the frequency and Z'' is the imaginary part of the measured impedance. This relation assumes that the real part of the impedance, Z', is negligible at low frequencies.

The average capacitance values for each composition were calculated based on at least 5 different samples.

4.6. Vapor-Phase Infiltration (VPI) and High-Resolution Scanning Electron Microscopy (HRSEM)

For VPI, HRSEM, Si substrates (n-doped ⟨100⟩ silicon wafers, resistivity of 0.001–0.005 Ohm cm, single-side polished, Nova electronic materials, USA) were cleaned and spin-coated as described above. The VPI procedure was performed using an atomic layer deposition system (ALD) (Ultratech/Cambridge Nanotech Savannah, Veeco Instruments Inc.) at a temperature

of 60 °C through 80 alternating pulses of diethylzinc (DEZ) and deionized (DI) water, with nitrogen as carrier and purge gas. Each cycle included two DEZ pulses (0.02 s pulse +20 s hold +25 s purge) and two DI water pulses (0.04 s pulse +20 s hold +25 s purge). The flow rate of the reactor was 20 sccm.

After VPI, the samples were cleaved in liquid nitrogen to form sharp cross-section samples. HRSEM micrographs were taken using a Zeiss Ultra-Plus FEG-SEM operated at 1.5 kV accelerating voltage with a working distance of ~ 2.7 mm. The backscattered electron signal (BSE detector) and secondary electron signal (In lens detector) were collected simultaneously.

4.7. Grazing Incidence Wide-Angle X-Ray Scattering (GIWAXS)

GIWAXS measurements of silicon-coated substrates were performed using a Rigaku SmartLab 9 kW X-ray diffractometer with Cu Kα radiation ($\lambda = 1.54186$ Å), equipped with a HyPix-3000 2D detector, and with an installed aperture slit and reflection attachment head. The measurements were recorded at an incident angle of $\omega = 0.19°$.

Author contributions

The manuscript was written through contributions of all authors. All authors have given approval to the final version of the manuscript.

Conflicts of interest

The authors declare no competing financial interest.

Data availability

All data supporting the findings of this study are available within the article and its supplementary information (SI). Supplementary information is available. See DOI: **https://doi.org/10.1039/d5tc03284a**.

Acknowledgements

References

1 J. Rivnay, R. M. Owens and G. G. Malliaras, The Rise of Organic Bioelectronics, *Chem. Mater.*, 2014, **26**(1), 679–685, DOI: **10.1021/cm4022003**.

2 B. D. Paulsen, K. Tybrandt, E. Stavrinidou and J. Rivnay, Organic Mixed Ionic–Electronic Conductors, *Nat. Mater.*, 2020, **19**(1), 13–26, DOI: **10.1038/s41563-019-0435-z**.

3 S. Fabiano, L. Flagg, T. C. Hidalgo Castillo, S. Inal, L. G. Kaake, L. V. Kayser, S. T. Keene, S. Ludwigs, C. Muller, B. M. Savoie, B. Lüssem, J. L. Lutkenhaus, M. Matta, D. Meli,

This journal is © The Royal Society of Chemistry 2026

J. Mater. Chem. C, 2026, **14**, 1164–1176 | **1173**

S. N. Patel, B. D. Paulsen, J. Rivnay and J. Surgailis, On the Fundamentals of Organic Mixed Ionic/Electronic Conductors, *J. Mater. Chem. C*, 2023, **11**(42), 14527–14539, DOI: **10.1039/d3tc03058j**.

4 J. Rivnay, S. Inal, A. Salleo, R. M. Owens, M. Berggren and G. G. Malliaras, Organic Electrochemical Transistors, *Nat. Rev. Mater.*, 2018, **3**(2), 17086, DOI: **10.1038/natrevmats.2017.86**.

5 S. Inal, G. G. Malliaras and J. Rivnay, Benchmarking Organic Mixed Conductors for Transistors, *Nat. Commun.*, 2017, **8**(1), 1767, DOI: **10.1038/s41467-017-01812-w**.

6 A. Giovannitti, D. T. Sbircea, S. Inal, C. B. Nielsen, E. Bandiello, D. A. Hanifi, M. Sessolo, G. G. Malliaras, I. McCulloch and J. Rivnay, Controlling the Mode of Operation of Organic Transistors through Side-Chain Engineering, *Proc. Natl. Acad. Sci. U. S. A.*, 2016, **113**(43), 12017–12022, DOI: **10.1073/pnas.1608780113**.

7 A. Giovannitti, I. P. Maria, D. Hanifi, M. J. Donahue, D. Bryant, K. J. Barth, B. E. Makdah, A. Savva, D. Moia, M. Zetek, P. R. F. Barnes, O. G. Reid, S. Inal, G. Rumbles, G. G. Malliaras, J. Nelson, J. Rivnay and I. McCulloch, The Role of the Side Chain on the Performance of N-Type Conjugated Polymers in Aqueous Electrolytes, *Chem. Mater.*, 2018, **30**(9), 2945–2953, DOI: **10.1021/acs.chemmater. 8b00321**.

8 P. Schmode, A. Savva, R. Kahl, D. Ohayon, F. Meichsner, O. Dolynchuk, T. Thurn-Albrecht, S. Inal and M. Thelakkat, The Key Role of Side Chain Linkage in Structure Formation and Mixed Conduction of Ethylene Glycol Substituted Polythiophenes, *ACS Appl. Mater. Interfaces*, 2020, **12**(11), 13029–13039, DOI: **10.1021/acsami.9b21604**.

9 S. E. Chen, L. Q. Flagg, J. W. Onorato, L. J. Richter, J. Guo, C. K. Luscombe and D. S. Ginger, Impact of Varying Side Chain Structure on Organic Electrochemical Transistor Performance: A Series of Oligoethylene Glycol-Substituted Polythiophenes, *J. Mater. Chem. A*, 2022, 10738–10749, DOI: **10.1039/d2ta00683a**.

10 L. Q. Flagg, C. G. Bischak, J. W. Onorato, R. B. Rashid, C. K. Luscombe and D. S. Ginger, Polymer Crystallinity Controls Water Uptake in Glycol Side-Chain Polymer Organic Electrochemical Transistors, *J. Am. Chem. Soc.*, 2019, **141**(10), 4345–4354, DOI: **10.1021/jacs.8b12640**.

11 A. A. Szumska, I. P. Maria, L. Q. Flagg, A. Savva, J. Surgailis, B. D. Paulsen, D. Moia, X. Chen, S. Griggs, J. T. Mefford, R. B. Rashid, A. Marks, S. Inal, D. S. Ginger, A. Giovannitti and J. Nelson, Reversible Electrochemical Charging of N-Type Conjugated Polymer Electrodes in Aqueous Electrolytes, *J. Am. Chem. Soc.*, 2021, **143**(36), 14795–14805, DOI: **10.1021/jacs.1c06713**.

12 M. Barker, T. Nicolini, Y. A. Yaman, D. Thuau, O. Siscan, S. Ramachandran, E. Cloutet, C. Brochon, L. J. Richter, O. J. Dautel, G. Hadziioannou and N. Stingelin, Conjugated Polymer Blends for Faster Organic Mixed Conductors, *Mater. Horiz.*, 2022, **10**(1), 248–256, DOI: **10.1039/d2mh00861k**.

13 S. R. Jackson, G. W. Collins, T. D. U. Phan, J. F. Ponder and C. G. Bischak, Enhancing N-Type Organic Electrochemical Transistor Performance via Blending Alkyl and Oligoglycol Functionalized Polymers, *Adv. Mater.*, 2025, **37**(40), e05963, DOI: **10.1002/adma.202505963**.

14 H. Frankenstein, E. Stein, M. Stolov, M. Koifman Khristosov, V. Freger and G. L. Frey, Blends of Polymer Semiconductor and Polymer Electrolyte for Mixed Ionic and Electronic Conductivity, *J. Mater. Chem. C*, 2021, **9**(24), 7765–7777, DOI: **10.1039/d1tc00916h**.

15 X. Wu, T. L. D. Tam, S. Chen, T. Salim, X. Zhao, Z. Zhou, M. Lin, J. Xu, Y. L. Loo and W. L. Leong, All-Polymer Bulk-Heterojunction Organic Electrochemical Transistors with Balanced Ionic and Electronic Transport, *Adv. Mater.*, 2022, **34**(42), 1–11, DOI: **10.1002/adma.202206118**.

16 E. Stein, O. Nahor, M. Stolov, V. Freger, I. M. Petruta, I. McCulloch and G. L. Frey, Ambipolar Blend-Based Organic Electrochemical Transistors and Inverters, *Nat. Commun.*, 2022, **13**(1), 5548, DOI: **10.1038/s41467-022-33264-2**.

17 N. Moscovich, S. Simotko, E. Reyn, I. Zerachia, A. Hadar and G. L. Frey, Balanced Ambipolar OECTs through Tunability of Blend Microstructure, *ACS Appl. Mater. Interfaces*, 2025, **17**(30), 43327–43338, DOI: **10.1021/acsami.5c05400**.

18 S. Simotko, Y. Yadav and G. L. Frey, A Blending Approach for Dual Surface and Bulk Functionality in Organic Transistors, *Adv. Electron. Mater.*, 2025, **11**(17), 2500085, DOI: **10.1002/aelm.202500085**.

19 Y. Hayashi, H. Kanamori, I. Yamada, A. Takasu, S. Takagi and K. Kaneko, Facile Fabrication Method for Pn -Type and Ambipolar Transport Polyphenylenevinylene-Based Thin-Film Field-Effect Transistors by Blending C60 Fullerene, *Appl. Phys. Lett.*, 2005, **86**(5), 1–3, DOI: **10.1063/1.1861115**.

20 Y. Zhang, D. Deng, K. Lu, J. Zhang, B. Xia, Y. Zhao, J. Fang and Z. Wei, Synergistic Effect of Polymer and Small Molecules for High-Performance Ternary Organic Solar Cells, *Adv. Mater.*, 2015, **27**(6), 1071–1076, DOI: **10.1002/adma. 201404902**.

21 E. Stein, S. Simotko, Y. Yadav, P. Cavassin, I. McCulloch, N. Banerji and G. L. Frey, Synergistic Effects in Ambipolar Blends of Mixed Ionic–Electronic Conductors, *Mater. Horiz.*, 2025, **12**(15), 5733–5748, DOI: **10.1039/D5MH00293A**.

22 C. J. Brabec, S. Gowrisanker, J. J. M. Halls, D. Laird, S. Jia and S. P. Williams, Polymer–Fullerene Bulk-Heterojunction Solar Cells, *Adv. Mater.*, 2010, **22**(34), 3839–3856, DOI: **10.1002/adma.200903697**.

23 M. T. Dang, L. Hirsch and G. Wantz, P3HT:PCBM, Best Seller in Polymer Photovoltaic Research, *Adv. Mater.*, 2011, **23**(31), 3597–3602, DOI: **10.1002/adma.201100792**.

24 N. Li, D. Baran, K. Forberich, F. Machui, T. Ameri, M. Turbiez, M. Carrasco-Orozco, M. Drees, A. Facchetti, F. C. Krebs and C. J. Brabec, Towards 15% Energy Conversion Efficiency: A Systematic Study of the Solution-Processed Organic Tandem Solar Cells Based on Commercially Available Materials, *Energy Environ. Sci.*, 2013, **6**(12), 3407–3413, DOI: **10.1039/C3EE42307G**.

25 C. G. Bischak, L. Q. Flagg, K. Yan, C. Z. Li and D. S. Ginger, Fullerene Active Layers for N-Type Organic Electrochemical Transistors, *ACS Appl. Mater. Interfaces*, 2019, **11**(31), 28138–28144, DOI: **10.1021/acsami.9b11370**.

1174 | *J. Mater. Chem. C*, 2026, **14**, 1164–1176

This journal is © The Royal Society of Chemistry 2026

26 R. Porrazzo, A. Luzio, S. Bellani, G. E. Bonacchini, Y. Y. Noh, Y. H. Kim, G. Lanzani, M. R. Antognazza and M. Caironi, Water-Gated n-Type Organic Field-Effect Transistors for Complementary Integrated Circuits Operating in an Aqueous Environment, *ACS Omega*, 2017, **2**(1), 1–10, DOI: **10.1021/acsomega.6b00256**.

27 A. A. Y. Guilbert, L. X. Reynolds, A. Bruno, A. MacLachlan, S. P. King, M. A. Faist, E. Pires, J. E. Macdonald, N. Stingelin, S. A. Haque and J. Nelson, Effect of Multiple Adduct Fullerenes on Microstructure and Phase Behavior of P3HT:Fullerene Blend Films for Organic Solar Cells, *ACS Nano*, 2012, **6**(5), 3868–3875, DOI: **10.1021/nn204996w**.

28 A. Levitsky, S. A. Schneider, E. Rabkin, M. F. Toney and G. L. Frey, Bridging the Thermodynamics and Kinetics of Temperature-Induced Morphology Evolution in Polymer/Fullerene Organic Solar Cell Bulk Heterojunction, *Mater. Horiz.*, 2021, **8**(4), 1272–1285, DOI: **10.1039/d0mh01805h**.

29 C. A. Reed and R. D. Bolskar, Discrete Fulleride Anions and Fullerenium Cations, *Chem. Rev.*, 2000, **100**(3), 1075–1120, DOI: **10.1021/cr980017o**.

30 S. Obuchovsky, H. Frankenstein, J. Vinokur, A. K. Hailey, Y.-L. Loo and G. L. Frey, Mechanism of Metal Oxide Deposition from Atomic Layer Deposition inside Nonreactive Polymer Matrices: Effects of Polymer Crystallinity and Temperature, *Chem. Mater.*, 2016, **28**(8), 2668–2676, DOI: **10.1021/acs.chemmater.6b00159**.

31 C. B. Nielsen, A. Giovannitti, D.-T. Sbircea, E. Bandiello, M. R. Niazi, D. A. Hanifi, M. Sessolo, A. Amassian, G. G. Malliaras, J. Rivnay and I. McCulloch, Molecular Design of Semiconducting Polymers for High-Performance Organic Electrochemical Transistors, *J. Am. Chem. Soc.*, 2016, **138**(32), 10252–10259, DOI: **10.1021/jacs.6b05280**.

32 M. Moser, L. R. Savagian, A. Savva, M. Matta, J. F. Ponder Jr., T. C. Hidalgo, D. Ohayon, R. Hallani, M. Reisjalali, A. Troisi, A. Wadsworth, J. R. Reynolds, S. Inal and I. McCulloch, Ethylene Glycol-Based Side Chain Length Engineering in Polythiophenes and Its Impact on Organic Electrochemical Transistor Performance, *Chem. Mater.*, 2020, **32**(15), 6618–6628, DOI: **10.1021/acs.chemmater.0c02041**.

33 T. C. Hidalgo Castillo, W. Shan, G. Ma, H. Zhao, Y. Wang, V. Druet, A. Saleh, X. Gu and S. Inal, Thermal Annealing for High Performance and Memory Behavior in N-Type Organic Electrochemical Transistors, *Adv. Mater.*, 2025, **37**(5), 2411214, DOI: **10.1002/adma.202411214**.

34 S. Holliday, J. E. Donaghey and I. McCulloch, Advances in Charge Carrier Mobilities of Semiconducting Polymers Used in Organic Transistors, *Chem. Mater.*, 2014, **26**(1), 647–663, DOI: **10.1021/cm402421p**.

35 S.-M. Kim, C.-H. Kim, Y. Kim, N. Kim, W.-J. Lee, E.-H. Lee, D. Kim, S. Park, K. Lee, J. Rivnay and M.-H. Yoon, Influence of PEDOT:PSS Crystallinity and Composition on Electrochemical Transistor Performance and Long-Term Stability, *Nat. Commun.*, 2018, **9**(1), 3858, DOI: **10.1038/s41467-018-06084-6**.

36 A. Savva, R. Hallani, C. Cendra, J. Surgailis, T. C. Hidalgo, S. Wustoni, R. Sheelamanthula, X. Chen, M. Kirkus, A. Giovannitti, A. Salleo, I. McCulloch and S. Inal, Balancing Ionic and Electronic Conduction for High-Performance Organic Electrochemical Transistors, *Adv. Funct. Mater.*, 2020, **30**(11), 1907657, DOI: **10.1002/adfm.201907657**.

37 E. Verploegen, C. E. Miller, K. Schmidt, Z. Bao and M. F. Toney, Manipulating the Morphology of P3HT-PCBM Bulk Heterojunction Blends with Solvent Vapor Annealing, *Chem. Mater.*, 2012, **24**(20), 3923–3931, DOI: **10.1021/cm302312a**.

38 E. Verploegen, R. Mondal, C. J. Bettinger, S. Sok, M. F. Toney and Z. Bao, Effects of Thermal Annealing Upon the Morphology of Polymer–Fullerene Blends, *Adv. Funct. Mater.*, 2010, **20**(20), 3519–3529, DOI: **10.1002/adfm.201000975**.

39 W. Wang, S. Guo, E. M. Herzig, K. Sarkar, M. Schindler, D. Magerl, M. Philipp, J. Perlich and P. Müller-Buschbaum, Investigation of Morphological Degradation of P3HT:PCBM Bulk Heterojunction Films Exposed to Long-Term Host Solvent Vapor, *J. Mater. Chem. A*, 2016, **4**(10), 3743–3753, DOI: **10.1039/c5ta09873d**.

40 P. Kohn, Z. Rong, K. H. Scherer, A. Sepe, M. Sommer, P. Müller-Buschbaum, R. H. Friend, U. Steiner and S. Hüttner, Crystallization-Induced 10-Nm Structure Formation in P3HT/PCBM Blends, *Macromolecules*, 2013, **46**(10), 4002–4013, DOI: **10.1021/ma400403c**.

41 E. von Hauff, J. Parisi and V. Dyakonov, Field Effect Measurements on Charge Carrier Mobilities in Various Polymer-Fullerene Blend Compositions, *Thin Solid Films*, 2006, **511–512**, 506–511, DOI: **10.1016/j.tsf.2005.12.025**.

42 L. Janasz, A. Luczak, T. Marszalek, B. G. R. Dupont, J. Jung, J. Ulanski and W. Pisula, Balanced Ambipolar Organic Field-Effect Transistors by Polymer Preaggregation, *ACS Appl. Mater. Interfaces*, 2017, **9**(24), 20696–20703, DOI: **10.1021/acsami.7b03399**.

43 S. Goffri, C. Müller, N. Stingelin-Stutzmann, D. W. Breiby, C. P. Radano, J. W. Andreasen, R. Thompson, R. A. J. Janssen, M. M. Nielsen, P. Smith and H. Sirringhaus, Multicomponent Semiconducting Polymer Systems with Low Crystallization- Induced Percolation Threshold, *Nat. Mater.*, 2006, **5**(12), 950–956, DOI: **10.1038/nmat1779**.

44 L. Qiu, X. Wang, W. H. Lee, J. A. Lim, J. S. Kim, D. Kwak and K. Cho, Organic Thin-Film Transistors Based on Blends of Poly(3-Hexylthiophene) and Polystyrene with a Solubility-Induced Low Percolation Threshold, *Chem. Mater.*, 2009, **21**(19), 4380–4386, DOI: **10.1021/cm900628j**.

45 V. Coropceanu, J. Cornil, D. A. da Silva Filho, Y. Olivier, R. Silbey and J.-L. Brédas, Charge Transport in Organic Semiconductors, *Chem. Rev.*, 2007, **107**(4), 926–952, DOI: **10.1021/cr050140x**.

46 S. Wang, M. Ha, M. Manno, C. Daniel Frisbie and C. Leighton, Hopping Transport and the Hall Effect near the Insulator-Metal Transition in Electrochemically Gated Poly(3-Hexylthiophene) Transistors, *Nat. Commun.*, 2012, **3**, 1210, DOI: **10.1038/ncomms2213**.

This journal is © The Royal Society of Chemistry 2026

J. Mater. Chem. C, 2026, **14**, 1164–1176 | 1175

47 H. Liao, J. Chen, L. Lan, Y. Yu, G. Zhu, J. Duan, X. Zhu, H. Dai, M. Xiao, Z. Li, W. Yue and I. McCulloch, Efficient N-Type Small-Molecule Mixed Ion-Electron Conductors and Application in Hydrogen Peroxide Sensors, *ACS Appl. Mater. Interfaces*, 2022, **14**(14), 16477–16486, DOI: **10.1021/acsami.1c24267**.

48 M. Sessolo, D. Khodagholy, J. Rivnay, F. Maddalena, M. Gleyzes, E. Steidl, B. Buisson and G. G. Malliaras, Easy-to-Fabricate Conducting Polymer Microelectrode Arrays, *Adv. Mater.*, 2013, **25**(15), 2135–2139, DOI: **10.1002/adma.201204322**.